Applied Surface Science 457 (2018) 942–955

Contents lists available at ScienceDirect

Applied Surface Science

journal homepage: www.elsevier.com/locate/apsusc

Full Length Article

Investigation of wear behavior of as-plated and plasma-nitrided Ni-B-CNT electroless having different CNTs concentration

S. Yazdani*, R. Tima, F. Mahboubi

Department of Mining and Metallurgical Engineering, Amirkabir University of Technology, Hafez Ave, P.O. Box, 15875-4413 Tehran, Iran

ARTICLE INFO

Keywords:
Ni-B electroless
Plasma nitriding
Wear
Carbon nanotubes

ABSTRACT

In the present study, the wear behavior of as-plated and plasma-nitrided Ni-B-CNT coatings was taken into investigation. Ni-B-CNT composite was deposited on AISI 4140 steel using different concentration of CNTs ranging from 0.2 to 1 $g{\cdot}L^{-1}$, in an electroless bath. After the plating process, all samples were plasma nitrided in an atmosphere comprising of 25%N_2-75% H_2, at 400 °C, for 4 h. The friction and wear behavior of the composite coatings were evaluated using a pin on disk method at an applied load of 10 N. The samples were then characterized by means of XRD, FESEM, microhardness and surface roughness measurements. Worn surfaces were further analyzed by FESEM and EDS spectroscopy. Microhardness results revealed that the maximum hardness of 1550 HV was obtained for Ni-B 0.6 $g{\cdot}L^{-1}$ CNT plasma-nitrided sample. According to the results, increasing the CNTs concentration caused the as-plated Ni-B amorphous structure to change to semi-crystalline. Furthermore, the crevices formed during the hydrogen evolution reaction were observed to be filled up. Presence of CNTs not only decreased the grain size in the plasma-nitrided samples but also prevented excessive heat generation during the wear test, and thus the friction coefficient was declined during the test. Moreover, image of the worn surface of Ni-B 0.6 $g{\cdot}L^{-1}$ CNT plasma-nitrided sample indicated the smoothest wear trace with no apparent cracks and the highest wear resistance among all the samples was achieved. While, in Ni-B-1 $g{\cdot}L^{-1}$ CNT sample, agglomeration created asperities as well as large particles weakly bonded to the Ni matrix which ultimately led to an increase in the specific wear rate.

1. Introduction

Electroless coating is an autocatalytic deposition process which has been widely utilized in the industry due to its cost-effectiveness, uniform coating and less complex process [1,2]. The Ni electroless plating is divided into three different extended groups: pure Ni, Ni-P, and Ni-B. The coating process for each of these groups is carried out within a bath containing different reduction agent, hydrazine is used for Ni, hypophosphite for Ni-P and sodium borohydride or dimethylamine borane for Ni-B. The tribological behavior of Ni-B coating has been markedly noticed as a result of its excellent mechanical properties and high wear resistance [3–7]. The unique properties of Ni-B make it a promising candidate for utilization in aerospace, petroleum, automotive and plastic applications as well as textile industry [1,7–11]. The most common method to induce crystallization and enhance the coating hardness after the deposition process, is heat treatment in 95%Ar-5%H_2 atmosphere [3,5,9,12,13]. Only a handful of researchers have studied Ni-B heat treatment in a vacuum and nitriding atmosphere [14]. To achieve enhanced mechanical properties, corrosion resistance and wear resistance, composite and nanocomposite coatings have attracted a great deal of attention. Hard particles like diamond [15], SiC [11], TiO_2 [16], WC [17] and Al_2O_3 [18] have been widely applied in composite coatings in recent years. However, crack formation which tend to appear between the particles and the matrix after the heat treatment process, is considered the most common problem regarding such hard particles. Another category of composite or nanocomposite coating is known as solid lubricants such as graphite [19], MoS_2 [20], PTFE [10] and CNT [21,22] which could serve to decrease the coefficient of friction and improve the wear resistance of the surface.

Carbon nanotubes (CNTs) are graphene sheets rolled into cylinders. The walls of the tubes are hexagonal carbon with strong SP2 covalent carbon bonds, and the end caps contain pentagonal rings [23–26]. Owing to their strikingly high tensile strength and elastic modulus [27], they have attracted abundant attention in the field of metallic composites and ceramic composites and have been applied in Al-CNT [24], Cu-CNT [28], Ni-CNT [29] as well as Al_2O_3-CNT [30], ZrO_2-CNT [31] and Ni-P-CNT [32].

The high length-to-diameter ratio of CNTs has led to a major

* Corresponding author.
E-mail address: sepehr.yazdani@aut.ac.ir (S. Yazdani).

https://doi.org/10.1016/j.apsusc.2018.07.020
Received 10 May 2018; Received in revised form 21 June 2018; Accepted 3 July 2018
Available online 04 July 2018
0169-4332/

Table 1
Chemical composition of AISI 4140 steel.

Element	Fe	C	Cr	Si	Mn	Mo	S	P
wt%	balance	0.42	0.96	0.32	0.78	0.17	0.02	0.02

Table 2
Process parameters of plasma nitriding treatment.

Temperature	Time	Gas ratio	Duty cycle	Frequency
400 °C	4 h	75%H_2-25%N_2	70%	8.9 kHz

drawback which is their poor dispersion in solutions which causes agglomeration and led to an undesirable mechanical and tribological behavior of the coated surface. Mechanical treatments like ball-milling process and chemical treatment, including adding polymers, surfactants and oxidation of the CNTs, are the most common approaches taken to tackle their poor dispersion issue [33–35].

Surfactants are divided into the ionic and non-ionic groups. The ionic category, including anionic and cationic groups, creates repulsion force between the CNTs and therefore, their dispersibility grows. Application of non-ionic surfactants due to their hydrophilic ends is also considered for improving CNTs dispersibility [35–37].

Another effective approach taken to enhance the dispersion of CNTs is their oxidation which is conducted by inserting functional groups like carboxyl, carbonyl, lactonic, phenolic, aldehyde and hydroxyl on their sidewalls. The oxidation can be carried out by immersing CNTs into a solutions containing oxidizing agents such as H_2SO_4, HNO_3, H_2SO_4/HNO_3 and $KMnO_4$/H_2SO_4 [38–40].

The aim of the present study is to understand the effect of plasma nitriding treatment on the wear behavior of Ni-B-CNT electroless deposition. Furthermore, the effects of different concentrations of CNTs on the microhardness, crystallographic structure and wear behavior of the as-plated and plasma-nitrided samples were investigated.

2. Materials and methods

2.1. Substrate preparation

In this work, cylindrical samples (20 mm diameter × 10 mm height) made from AISI 4140 steel were used as the substrate. The chemical composition of the steel obtained by spark emission spectroscopy is shown in Table 1. In order to improve the mechanical properties such as hardness and toughness, the substrates were austenitized at 850 °C for 30 min followed by oil quenching. Then, they were tempered at 560 °C for 60 min. The samples surfaces were fine-ground using 100–800 grit SiC papers. Before the deposition, all samples were degreased in alkaline solution (10 wt% NaOH) to remove organic contaminates and then were cleaned using distilled water. Just a few second before the deposition, the samples were pickled in dilute HCl acid to remove all the existing oxidation products. They were subsequently cleaned using distilled water.

2.2. CNT ball-milling and functionalizing

Pristine CVD-grown Multi walled carbon nanotubes (MWCNT) with 95% purity, 10–30 μm in length and 10–20 nm in outside diameter, were purchased from US Research Nanomaterials, Inc. They were ball-milled for 2 h using a planetary ball-mill machine with spherical ZrO_2 balls (radius: 5 mm, weight: 3 g) and a 250 cc cylindrical stainless steel jar. The ball to powder ratio was kept at 20:1, with a rotating speed of 300 rpm and 5 min break intermitting every 10 min of milling to limit any heat build-up.

Finally, the samples were immersed in HNO_3/H_2SO_4 (volumetric 1:3) solution for 3 h in ultrasonic apparatus (Euronda 4D, 350 W). Then, they were collected on 0.2 μm filter paper, using vacuum filter and rinsed with distilled water until the acidity of the solution was neutralized. The final product was dried in a vacuum oven at 100 °C under 10^{-1} torr pressure, overnight.

2.3. Electroless bath preparation

The Ni–B coating was deposited on AISI 4140 steel by an electroless plating process. The bath was composed of 25 g·L^{-1} nickel chloride hexahydrate ($NiCl_2$·$6H_2O$), 30 cc·L^{-1} ethylenediamine ($C_2H_8N_2$) as the complexing agent, 0.02 g·L^{-1} Lead nitrate ($Pb(NO_3)_2$) as the stabilizer, 39 g·L^{-1} NaOH as the alkalinity reserve agent and 0.6 g·L^{-1} $NaBH_4$ as the reducing agent. The volume of the plating bath was 500 cc. The pH value of the plating bath was adjusted around 14. The electroless Ni–B plating was performed at 95 ± 1 °C for 60 min. During plating the bath solution was agitated using a mechanical stirrer at 500 rpm to minimize the fluctuation of ionic concentration and to prevent localized overheating. The sample was rotated in two opposite directions alternatively every 2 min to obtain uniform coating thickness. Considering the coating process, for Ni-B-CNT deposition with different concentration of the CNTs (0.2 g·L^{-1}, 0.6 g·L^{-1}, 1 g·L^{-1} CNT), CNTs were firstly

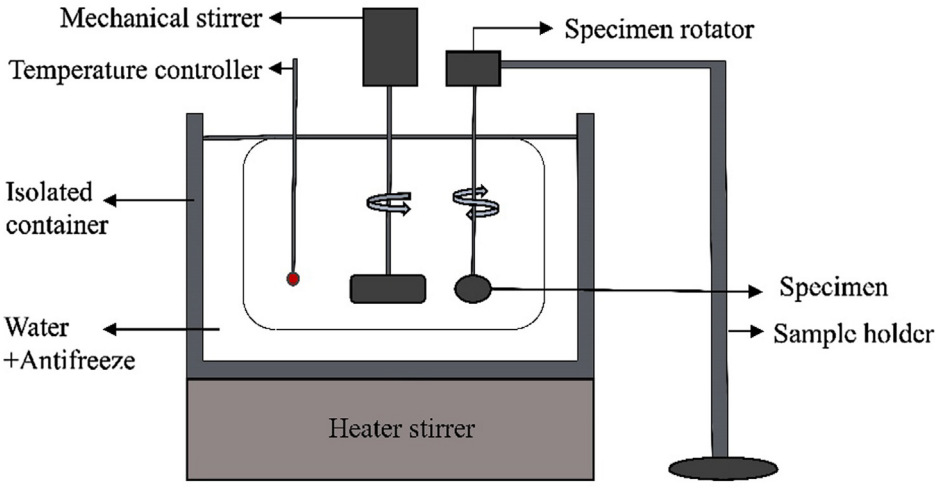

Fig. 1. Experimental setup for electroless deposition.

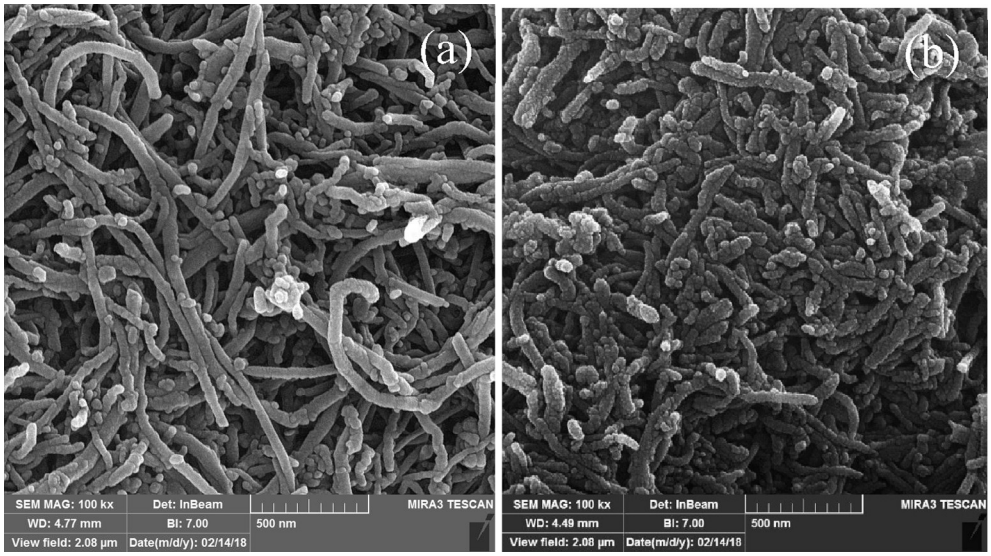

Fig. 2. SEM images of the (a) pristine CNT powders and (b) ball-milled CNT powders.

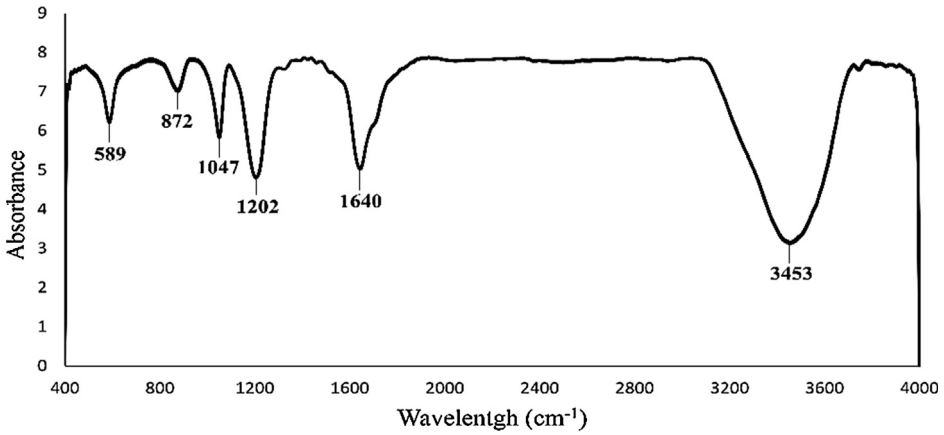

Fig. 3. FTIR spectra of functionalized CNTs.

dispersed in an ultrasonic bath and were subsequently added to the Ni-B prepared bath. A fresh electroless bath was applied for each test. Fig. 1 illustrates the experimental setup for the electroless composite deposition.

2.4. Plasma nitriding

After the deposition, all samples (Ni-B, Ni-B-0.2 $g{\cdot}L^{-1}$ CNT, Ni-B-0.6 $g{\cdot}L^{-1}$ CNT, Ni-B-1 $g{\cdot}L^{-1}$ CNT) were degreased using acetone and then were placed in a 5 kW conventional direct current plasma enhanced chemical vapor deposition (PECVD) chamber. The vacuum chamber was pumped down to 10^{-2} torr. Afterwards, the samples were plasma-nitrided at 400 °C for 4 h in a range of 500–700 V discharge voltage and 2–3 A current and under specified conditions described in Table 2.

At the end of the treatment, samples were slowly cooled in the chamber to reach the room temperature.

2.5. Characterization

The length and structure of CNTs before and after the ball-milling process as well as the thicknesses and morphologies of the composite coatings were studied, using MIRA3 TESCAN field emission scanning electron microscopy (FESEM). The functional group characterization of CNTs after oxidation was also analyzed by attenuated total reflection fourier transform infrared spectrometer (FTIR). To prepare the samples, CNTs were mechanically mixed with KBr powder and then the resultant powder was pressed to form a disc. FT-IR spectrum of CNTs was recorded in the range of 4000–400 cm^{-1} wavelength. EQuinox 3000 X-ray diffraction (XRD), with Cu K_α ($\lambda = 1.54187$ Å) radiation and scanning range of 2θ between 5° and 118° and operated at 40 kV and 30 mA was utilized to identify the crystal structure of the samples before and after the plasma nitriding treatment.

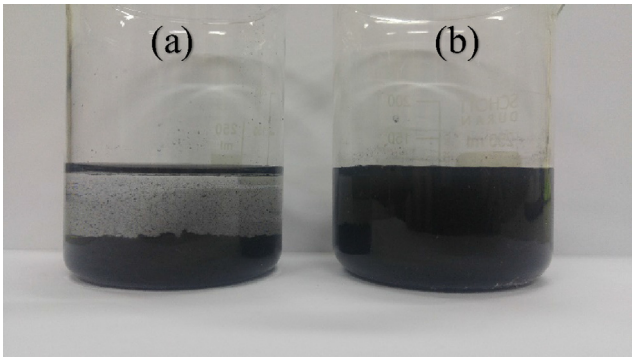

Fig. 4. Aqueous suspensions stability of (a) pristine CNT, (b) acid treated CNT.

The microhardness of the surface was measured for each samples

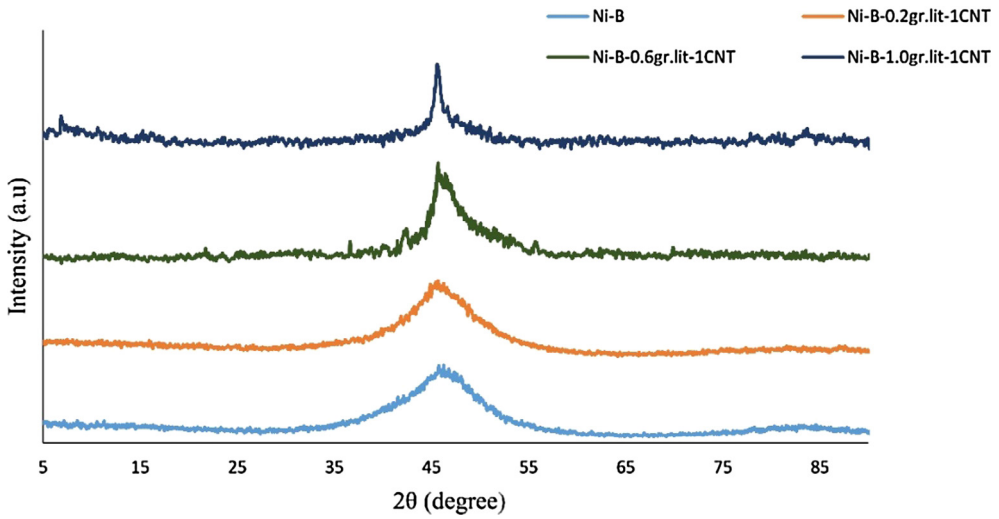

Fig. 5. X-ray diffraction patterns of as-plated Ni-B and Ni-B-CNT samples.

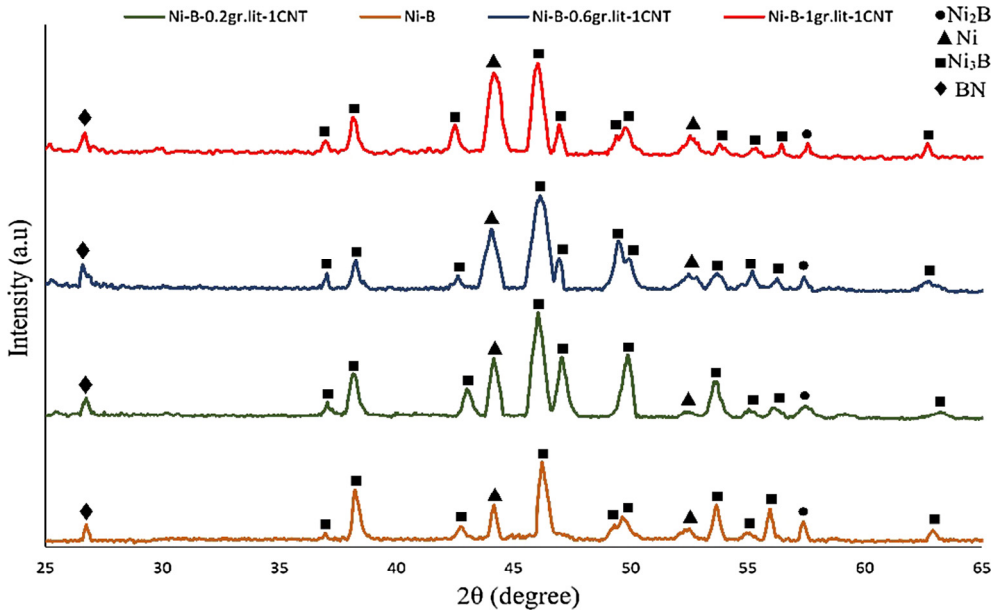

Fig. 6. X-ray diffraction patterns of plasma-nitrided Ni-B and Ni-B-CNT samples.

using a Shimadzu tester at a load of 50 g. The lap time for each indentation was 15 s. The reported value represents the average and standard deviation of five measurements. Surface roughness measurement was carried out for the coated samples using a Hand-held Roughness Tester TR200 and the average of ten measurements was recorded. Wear tests were performed on a pin-on-disk wear tester device with a horizontal rotating disc and a dead-loaded pin according to ASTM G 99 standard. The device applies a controlled load to the pin holder and create a circle wear track on the samples' surface. The pin was AISI 52100 steel with a 5 mm diameter semi-spherical end and hardness of 62 HRC. The conditions under which the dry wear tests were performed are a vertical load of 10 N, sliding speed of 0.05 m·min^{-1}, sliding distance of 500 m, and wear track radius of 7 mm at room temperature (25 °C) and relative humidity of about 40%. The diagrams of the friction coefficient to distance were drawn automatically by a device. The worn surface of the samples was investigated by applying FESEM and EDS spectroscopy. The mass loss was calculated by weighing the samples before and after the wear tests using an A&D Weighing GR-300 lab balance with an accuracy of up to 0.1 mg. The specific wear rates were calculated according to Eq. (1).

Table 3
Crystallite size and FWHM of plasma-nitrided samples.

Samples	Ni (1 1 1) FWHM	Ni (1 1 1) crystal size (nm)	Ni_3B (0 3 1) FWHM	Ni_3B (0 3 1) crystal size (nm)
Ni-B	0.2834	86.29	0.4408	34.71
Ni-B-0.2 g·L^{-1} CNT	0.3779	45.08	0.6298	19.27
Ni-B-0.6 g·L^{-1} CNT	0.4408	34.21	0.6927	17.66
Ni-B-1 g·L^{-1} CNT	0.3779	45.08	0.5353	25.48

$$w_s = w/(d \times F) \quad (1)$$

where w_s is the wear rate, w is the mass loss, F is the normal load and d is the siding distance.

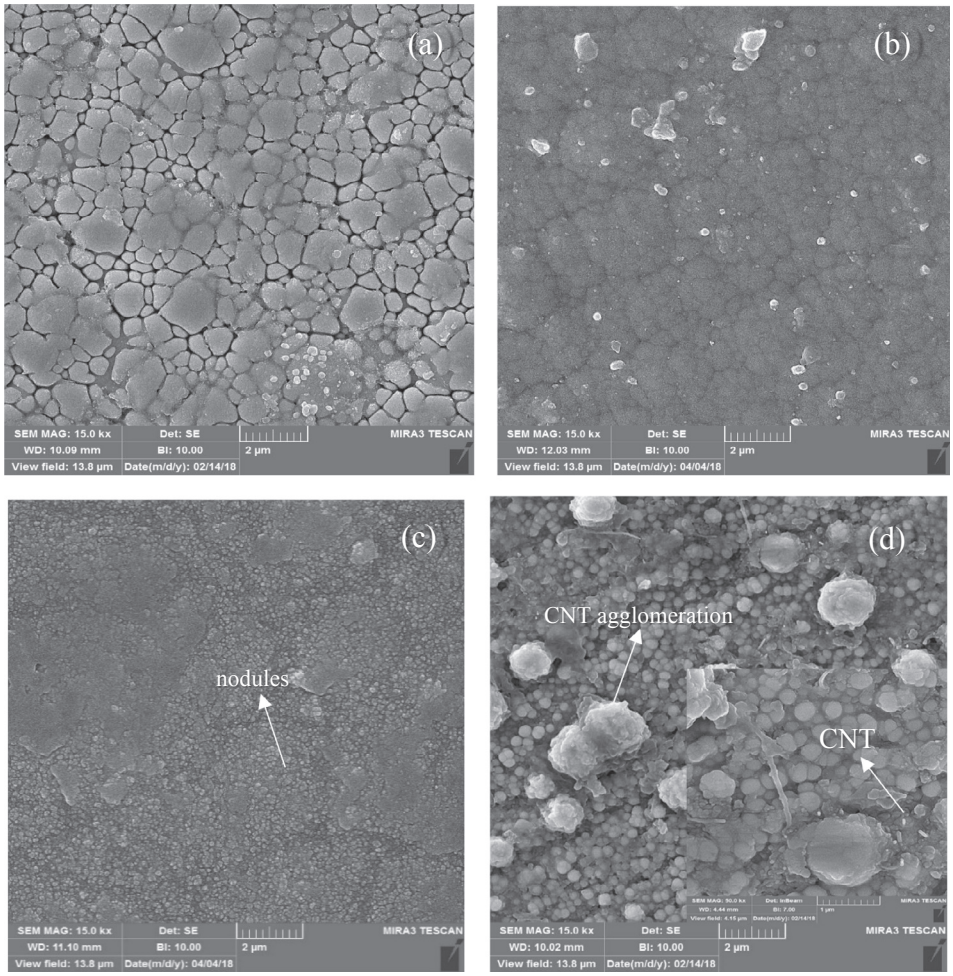

Fig. 7. FSEM images of electroless coated (a) Ni-B, (b) Ni-B-0.2 $g{\cdot}L^{-1}$ CNT, (c) Ni-B-0.6 $g{\cdot}L^{-1}$ CNT, (d) Ni-B-1 $g{\cdot}L^{-1}$ CNT surface.

3. Result and discussion

3.1. CNT characterization

As indicated in Fig. 2, the ball-milling process, significantly reduced the length of the carbon nanotubes. The high energy impact of the balls produced broken and sharp tips of nanotubes and thus their structure becomes less entangled [41,42].

Functionalization of the ball-milled CNTs in an ultrasonic bath would enhance the oxidation rate by providing high local shear force to the nanotube bundle end [43]. Nitronium ion (NO^{2+}) is the product of the reaction between sulfuric acid and nitric acid [44,45] which could attack and break some of the C═C bonds and also insert chemical groups such as hydroxyl, carboxylic and carbonyl on CNTs wall. The reaction can generate defects on CNTs wall or even make them shortened by cutting them into small pieces.

FTIR spectroscopy of acid treated CNTs in Fig. 3 reveals the different bonding types formed on CNTs surface during the functionalizing process. The broad peak at 3453 cm^{-1} wavelength could be associated with the stretching hydroxyls in the carboxyl groups. The peak at 1640 cm^{-1} wavelength is attributed to the carbonyl group, the peaks at 1202 cm^{-1} and 1047 cm^{-1} are related to C—OH and C—O—C chemical bonds [38,46]. Due to very low formation of electric dipoles in C═C bonding [40], the peak associated with this bonding was not observed.

Fig. 4 provides a comparison between dispersibility of ball-milled functionalized CNTs and the pristine CNTs in aqueous solution for a period of 24 h. As it can be observed, due to repulsive force between the negatively charged carbon nanotubes, the suspension of functionalized CNTs became stabilized. The strong tension of water in pristine CNTs is one of the factors that could hinder their dispersion [25].

3.2. XRD characterization

X-ray diffraction analysis of as-plated Ni-B shows a significantly broad peak around 45° corresponding to (1 1 1) plane of nickel phase, which indicates the amorphous nature of the coating (Fig. 5). The dominant (1 1 1) plane in the X-ray diffraction results is associated with the low surface energy of this plane [20]. Numerous researchers have reported an amorphous or semi-crystalline structure for as-plated Ni-B. Boron as an amorphous element prevents the nucleation of nickel phase [2]. By adding CNTs to the electroless bath, it was observed that the peak broadening was reduced and thus the peak became sharper as the CNTs concentration increased in the electroless bath. It can be concluded by the results in Ni-B-CNT samples H+ ions are released from carboxylic groups at the surface of CNTs and the remaining HCOO— ions act as a reducing agent and thus reduces the Ni ions. Therefore, Ni starts to nucleate on the crystal defects of CNTs which act as the nucleation site and the structure of as-plated Ni-B-CNT with increasing CNTs concentration became more semi-crystalline. Similar phenomena have been observed by adding SiC particles [11].

Fig. 6 shows the XRD patterns of plasma-nitrided samples. According to these patterns, after the plasma nitriding treatment, the structure of as-plated samples was changed from amorphous to crystalline state due to formation of Ni_2B and Ni_3B intermetallic compounds. It can be claimed that the presence of the Ni_3B phase is due to the decomposition of the unstable Ni_2B phase or it could be the result of

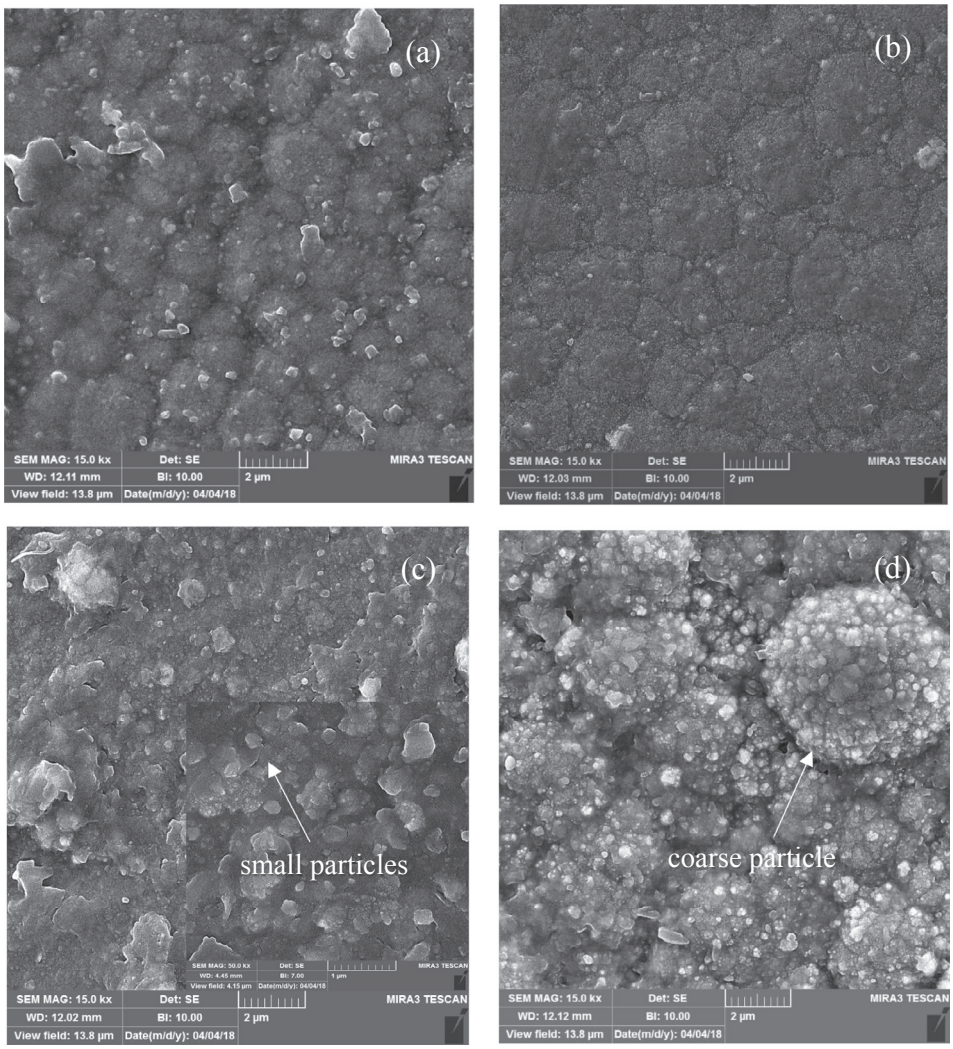

Fig. 8. FSEM images of plasma-nitrided (a) Ni-B, (b) Ni-B-0.2 $g{\cdot}L^{-1}$ CNT, (c) Ni-B-0.6 $g{\cdot}L^{-1}$ CNT, (d) Ni-B-1 $g{\cdot}L^{-1}$ CNT surface.

the asymmetric distribution of boron with low concentration. The presence of local concentrations of boron higher than 6% by weight has probably caused the Ni_2B phase formation to occur. Plus, continuous bombardment of the cathodic stage with the positively charged ions led to an increase in the surface temperature of samples and ultimately to the growth of the Ni_2B and Ni_3B phases.

The peak observed around 26° in all samples can probably be attributed to hexagonal boron nitride (BN) structure [14]. It can be claimed that sputtered boron atoms react with active nitrogen in plasma atmosphere and forms BN which is then deposited on the sample surface. For all samples, the XRD patterns illustrate that the Ni peak was shifted to lower angles. This change might be an indication of interstitial diffusion of the nitrogen atoms in the Ni matrix which could ultimately lead to an increase in the d-spacing by inducing the residual stress during the plasma nitriding process. Another reason could be the substitution of boron with nickel atoms during the treatment [47].

As can be noticed, the relative intensity of Ni (1 1 1)/Ni_3B (0 3 1) in the Ni-B-CNT coatings, around 45° was significantly increased as the CNTs concentration raised up to 1 $g{\cdot}L^{-1}$. This is probably due to the fact that CNTs act as the nucleation sites for Ni. This may facilitate the nucleation and thus cause the Ni peak intensity to rise in the diffractogram.

Due to low incorporation of CNTs, no CNT was detected in the diffractograms. Increasing CNTs concentration caused peak broadening to be observed which is the evidence of grain refinement. By applying Scherrer equation (Eq. (2)) on the XRD pattern, the calculation of the crystallite size was carried out. The final results are summarized in Table 3.

$$D = k \times \lambda/\beta_D \times \cos\theta \quad (k = 0.9) \tag{2}$$

where D is the crystallite size, λ is a wavelength (Cu K_α λ = 1.54187 Å), D is Scherrer's constant (in this case 0.9), β is peak broadening and θ is diffraction angle. To remove aberrations and line broadening of peaks, standard material (terbium oxide) was used to determine the instrumental broadening. The instrument-corrected broadening β_D peak was estimated using Eq. (3).

$$\beta_D^2 = \beta_{measures}^2 - \beta_{instrumental}^2 \tag{3}$$

As can be observed in Table 3, owing to the inhibition of crystal growth, by increasing the CNTs concentration the crystallite size was decreased. The crystallite size in Ni-B-0.6 $g{\cdot}L^{-1}$ CNT sample was found to be lower than the other samples. This could be due to the homogenous distribution of the CNTs in this sample in comparison with the others [48].

3.3. Surface morphology

The surface morphology of the as-plated samples is illustrated in Fig. 7. The smooth structure with some crevices and cracks can be observed in Ni-B sample image (Fig. 7a). The presence of crevices and

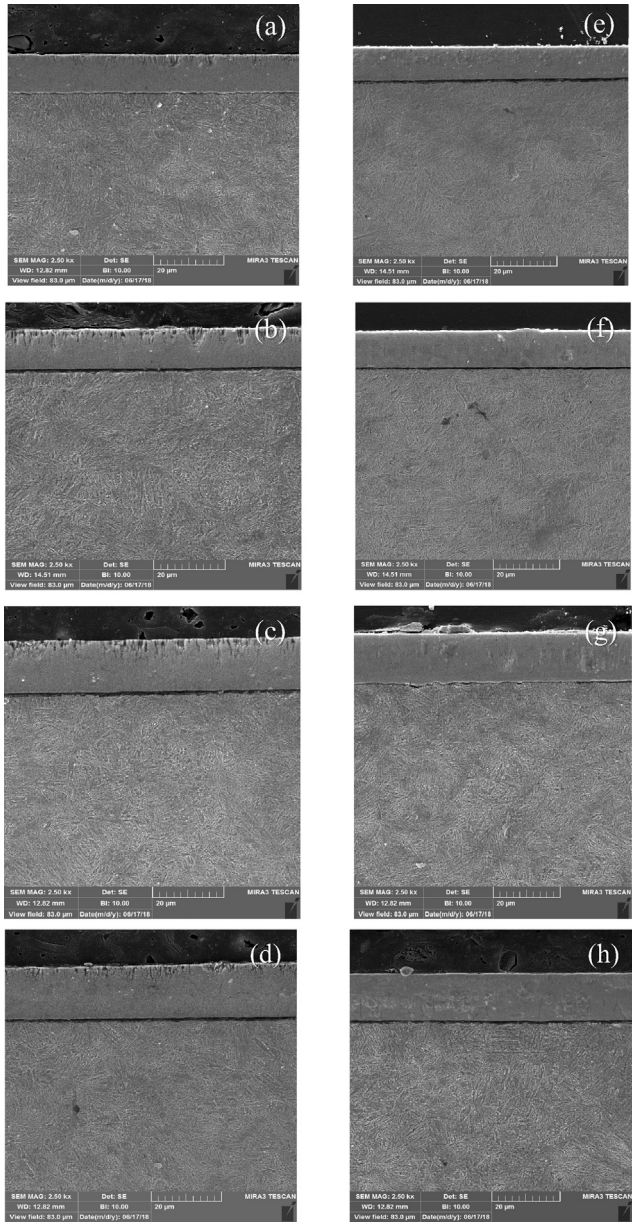

Fig. 9. Cross-sectional FESEM images of the (a) Ni-B, (b) Ni-B-0.2 g·L^{-1} CNT, (c) Ni-B-0.6 g·L^{-1} CNT, (d) Ni-B-1 g·L^{-1} CNT as-plated, and (e) Ni-B, (f) Ni-B-0.2 g·L^{-1} CNT, (g) Ni-B-0.6 g·L^{-1} CNT, (h) Ni-B-1 g·L^{-1} CNT plasma-nitrided samples.

Table 4
Results of samples surface roughness.

Sample	Ra (μm)
Substrate	0.02
Ni-B as-plated	0.04
Ni-B-0.2 g·L^{-1} CNT as-plated	0.09
Ni-B-0.6 g·L^{-1} CNT as-plated	0.15
Ni-B-1CNT as-plated	0.41
Ni-B plasma-nitrided	0.34
Ni-B-0.2 g·L^{-1} CNT plasma-nitrided	0.41
Ni-B-0.6 g·L^{-1} CNT plasma-nitrided	0.53
Ni-B-1CNT g·L^{-1} plasma-nitrided	0.71

cracks is a result of hydrogen evolution during the Ni-B deposition process. Some authors have reported that the main mechanism for the Ni-B electroless deposition is spontaneous catalytic oxidation of the reducing agent due to the activity of the substrate [49]. A more homogeneous particles distribution in the Ni matrix was observed by increasing the CNTs concentration from 0.2 g·L^{-1} to 0.6 g·L^{-1}. During the particle distribution, a bigger portion of the CNTs were embedded in the matrix while the smaller portion were protruded from the coated surface; However, CNTs were hardly observed at the surface of the samples containing 0.2 and 0.6 g·L^{-1} CNT, which could be due to the low concentration of CNTs (Fig. 7b, c). Moreover, in the sample containing 0.2 g·L^{-1} of CNTs, no significant change in the morphology was witnessed, which seems logical due to the low concentration of nanotubes. Raising the CNTs concentration up to 0.6 g·L^{-1} caused a more uniformly coated surface to be achieved since CNTs have the ability to fill the gaps and the crevices. By increasing the concentration of CNTs to 1 g·L^{-1}, the size of the nodules grew. This could be associated with the raised concentration of reduced Ni in the electroless bath which could cause the crystal growth to overshadow nucleation (Fig. 7d). The existence of large particles in Ni-B-1 g·L^{-1} CNT sample could be the result of the CNTs aggregation owing to the high concentration of them. The aggregation could lead to agglomeration of CNTs on the substrate and subsequently large particles at the surface of the samples could be formed owing to the nucleation of Ni on the agglomerated CNTs. In order to demonstrate the CNTs distribution more clearly, an image with higher magnification of the sample is also added to this figure (Fig. 7d).

According to Fig. 8, FESEM observations of the plasma-nitrided samples show that the surface morphology of Ni-B was changed into a cauliflower-like structure and became more densified (Fig. 8a). Similar observation has been made by numerous researchers after heat treatment in 95%Ar-5%H_2 atmosphere. The preferential deposition on defect sites of the surface at the beginning of the process might be the possible reason for the type of the structure seen [4,8,49]. In samples containing 0.2 and 0.6 g·L^{-1} CNT similar densification was occurred. In fact, the growth of crystals which were initially nucleated at different preferred sites has caused Ni_2B, Ni_3B, and BN particles to coincide and cover the surface of the sample. Also, sputtering and re-deposition of the atoms have possibly caused the re-deposited compounds to fill the holes during the plasma nitriding treatment. Higher magnification of the Ni-B-0.6 g·L^{-1} CNT sample shows homogenous distribution of small particles in comparison to other samples (Fig. 8c). This is probably due to the fact that, CNTs uniform distribution restricted the bonding between the particles by forming a barrier. The sample containing 1 g·L^{-1} CNT was consisted of coarser particles (Fig. 8d). The agglomerated particles were observed to become 2 or 3 times larger after the plasma nitriding treatment owing to high concentration of CNTs which causes more nucleation of the nanoclusters and more growth rate in this sample. However, no evidence of the CNTs at the surface of this sample was observed. This could be attributed to the fact that, the continuous ion bombardment during the plasma nitriding process has removed the excessive amount of CNTs from the surface.

Fig. 9 shows the FESEM images of cross-sections of as-plated and plasma-nitrided samples. Results of thickness indicates after plasma nitriding treatment the structure of samples becomes compact and denser without significant dimensional change. As reported by Vitry et al. [14] ammonia nitriding of as-plated Ni-B coating present a dual structure with a dense inner layer and a porous outer layer while vacuum nitriding presents a uniform dense layer. Results of Fig. 9 are in good agreement with their observation of vacuum-nitrided Ni-B sample. Moreover, increasing CNTs concentration caused higher thickness value of coated surface in both as-plated and plasma-nitrided samples, which indicated the deposition rate increases with increasing CNTs concentration.

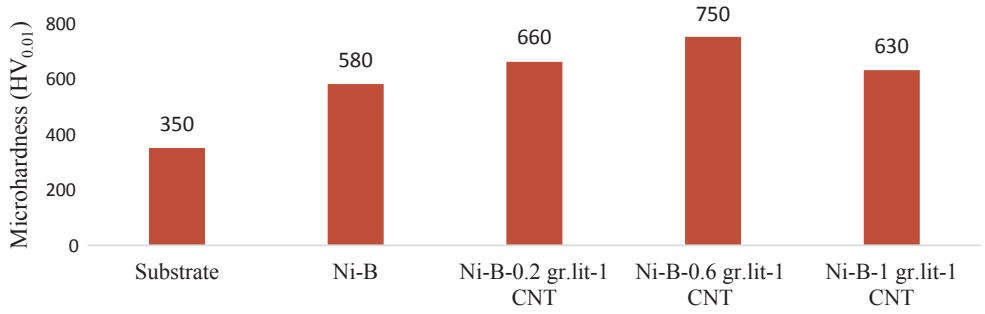

Fig. 10. Microhardness results of as-plated samples surface.

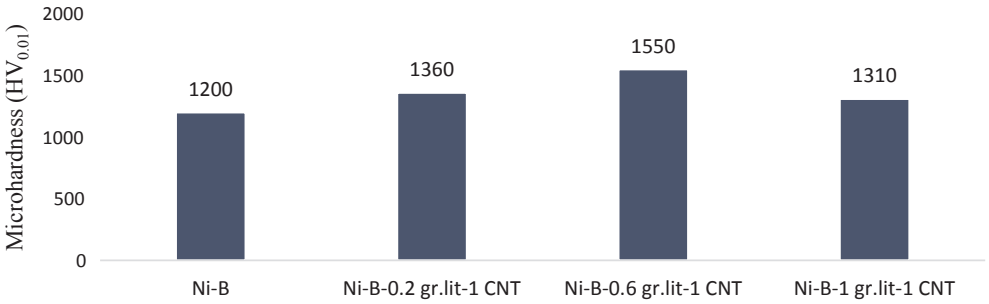

Fig. 11. Microhardness results of plasma-nitrided samples surface.

3.4. Surface roughness and microhardness

Table 4 provides data on the roughness of the substrate, as-plated and plasma-nitrided samples. As it is indicated, raising CNTs concentration up to 1 $g{\cdot}L^{-1}$ has led to a significant increase in the roughness. This is on the grounds that CNTs inhibit uniform growth of Ni and create asperities. In Ni-B-1 $g{\cdot}L^{-1}$ CNT sample the roughness was noticed to be much higher in comparison with the other samples, owing to the high concentration of CNTs which could causes agglomeration. After plasma nitriding, the roughness of all as-plated samples were increased. Three possible explanations could be provided for this result. First, after the plasma nitriding process, the crystal growth of Ni_2B, Ni_3B and BN phases in the Ni matrix created asperities and thus the surface roughness increased. Second, the sputtering effect during the plasma-nitriding process, caused by the positive nitrogen and hydrogen ion bombardment, affected the roughness of the samples. Third, this resulted due to the re-deposition of sputtered material on the surface.

Fig. 10 shows the surface microhardness of the as-plated samples. As can be observed, the reinforcing ability of CNTs had an impact on increasing the surface microhardness, especially in Ni-B-0.6 $g{\cdot}L^{-1}$ CNT sample. This can be attributed to the uniform distribution and reinforcement of CNTs in this sample. In Ni-B-1 $g{\cdot}L^{-1}$ CNT the hardness was found to be lower in comparison with the sample containing 0.6 $g{\cdot}L^{-1}$ CNT because of the higher concentration of CNTs, segregation which occurred in the composite caused a reduction in the microhardness of composite coated layer [50].

Fig. 11 illustrates the surface microhardness of the plasma-nitrided samples. After the plasma-nitriding process the value of microhardness increased. This is due to the formation of Ni_2B (between 5.8 and 8.5 wt % of B content), Ni_3B (less than 5.8 wt% of B content) and BN phases [5,9]. Grain refinement due to the presence of the CNTs could also be another reason for the high microhardness value of the coated surface [51]. Raising the concentration of CNTs up to 0.6 $g{\cdot}L^{-1}$, led to increase in microhardness; However, the microhardness value in Ni-B-1 $g{\cdot}L^{-1}$ CNT was observed to be decreased which could be attributed to the agglomeration of CNTs in this sample that led to a non-uniform particles distribution in Ni matrix and ultimately reduced the microhardness value of the coated surface.

3.5. Wear behavior

The diagrams of friction coefficient of as-plated samples are given in Fig. 12. A dramatic fluctuation of the friction coefficient was observed in Ni-B sample. This is associated with the high mutual solubility of iron and nickel which caused an increase in the contact area of the coated surface with the counterpart and also in high material removal. Another logical explanation for this behavior could be the crystallization of the amorphous coated sample during the wear test, due to the heat generation which can finally result in appearance of tensile stresses at the interface of amorphous and crystalline phases. Moreover, the cracks generated on the surface during the hydrogen evolution, led to stress concentration which facilitate delamination during the wear test and also increased fluctuation [7,32,47].

The coefficient of friction was decreased by raising the CNTs concentration up to 0.6 $g{\cdot}L^{-1}$ This might be ascribed to easy shear and rolling of lubricating carbon film that reduce the direct contact between the samples surface and the counterpart [21]. In Ni-B-1 $g{\cdot}L^{-1}$ CNT as-plated sample, at an initial distance of around 50 m, the coefficient of friction first increased and subsequently decreased (Fig. 12d). The reasons for this phenomenon is probably detachment of the agglomerated CNTs, in fact their poor cohesion with the Ni matrix led to an increase in wear rate of the sample. After that because of the oxide patches motion which could create a tribo-layer and CNTs rolling which acts as a separator, the coefficient of friction was declined [33].

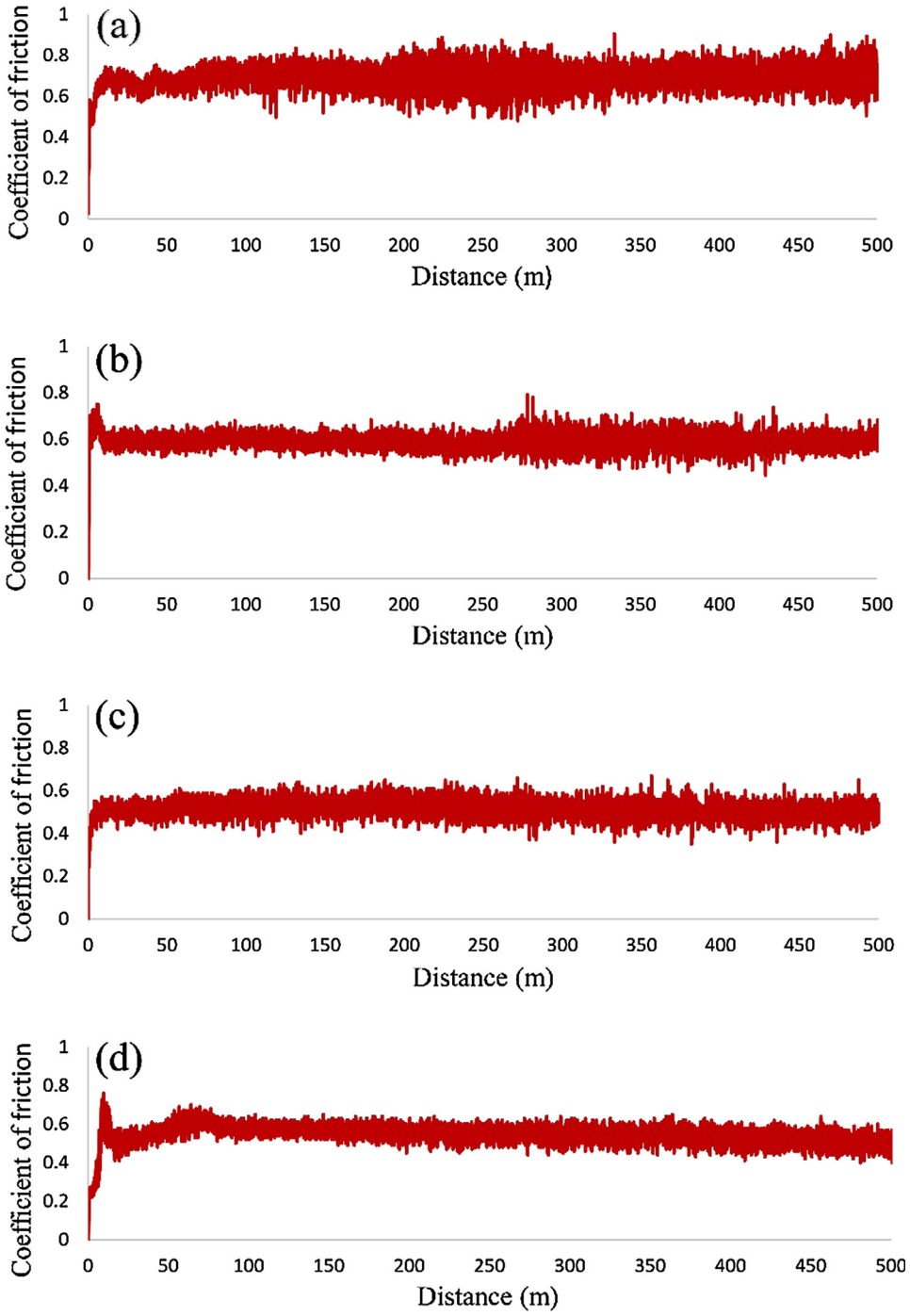

Fig. 12. Variations of the coefficient of friction against distance for (a) Ni-B, (b) Ni-B-0.2 g·L^{-1} CNT, (c) Ni-B-0.6 g·L^{-1} CNT, (d) Ni-B-1 g·L^{-1} CNT electroless coated samples.

Another factor which might effects samples wear behavior is surface roughness. Higher surface roughness could cause the abrasive interactions between the asperities on the surface of the Ni-B-1 g^{-1}·L CNT sample and the counterpart to be prevailed. Indeed, smaller contact area causes maximum local pressure between the pin and surface of the sample which resulted to higher wear rate and coefficient of friction. At the same time, in case of a lower coating roughness, the adhesive interaction between the pin and disc strongly grows which induces an increase in the friction coefficient as it is shown by the result of the friction coefficient for Ni-B as-plated sample.

Fig. 13 shows the friction coefficient diagrams of plasma-nitrided samples. In Ni-B sample after the plasma nitriding treatment, the coefficient of friction was markedly decreased. High microhardness value which requires more friction force for plastic deformation and also lower solubility of iron in Ni_2B, Ni_3B and BN particles are the reasons for this result. In Ni-B containing CNTs samples a similar

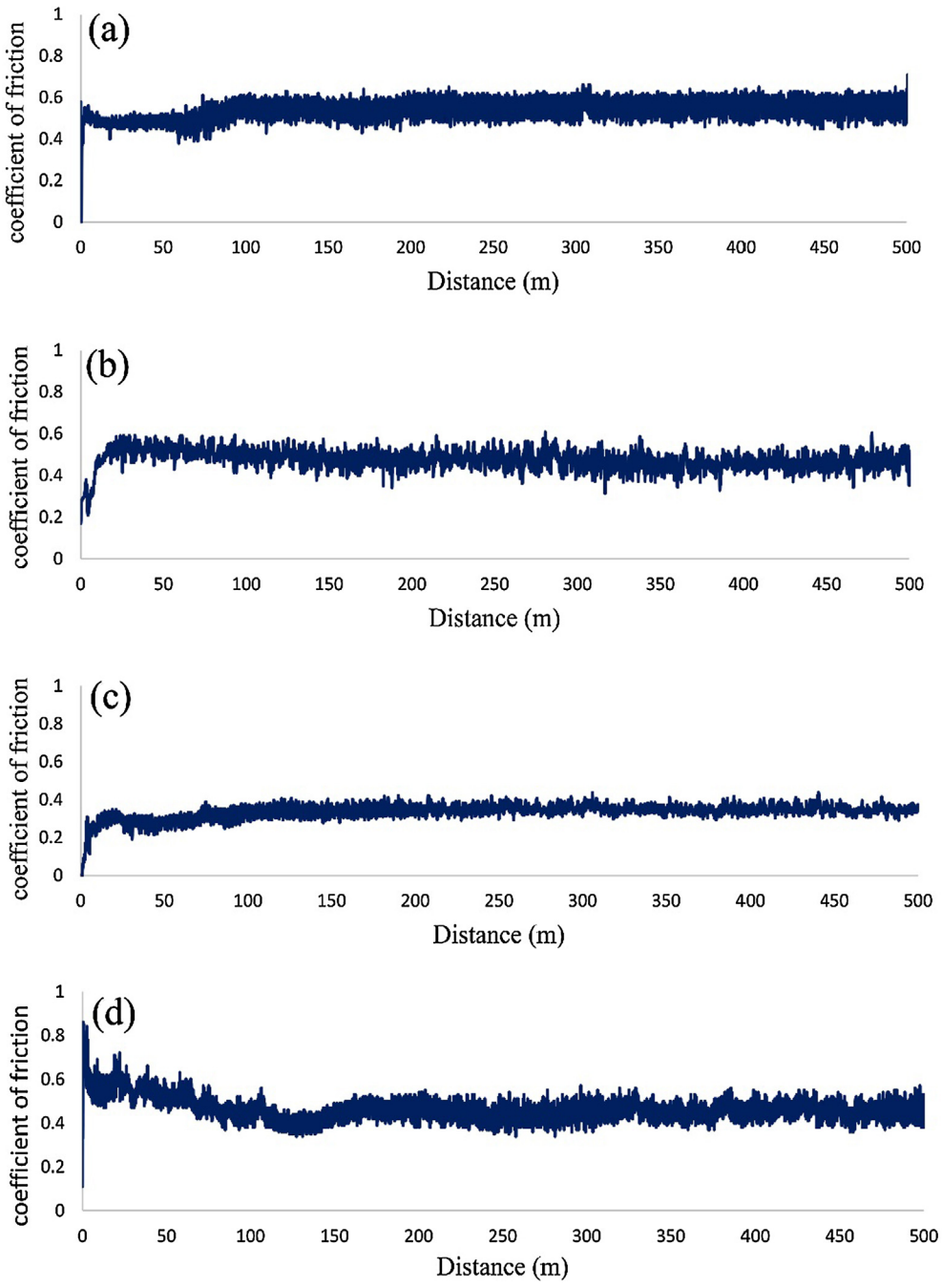

Fig. 13. Variations of the coefficient of friction against distance for (a) Ni-B, (b) Ni-B-0.2 g·L^{-1} CNT, (c) Ni-B-0.6 g·L^{-1} CNT, (d) Ni-B-1 g·L^{-1} CNT plasma-nitrided samples.

decreasing trend for the coefficient of friction was noticed after the plasma nitriding treatment. The basic causes for this behavior were firstly the increased microhardness value as well as the grain refinement. Secondly, the CNTs easily filled in the micro-holes of the surface during the electroless deposition process which are the active sites for tensile stress. Therefore, CNTs can prevent rapid plastic deformation. Thirdly, CNTs act as a major obstacle to the movement of dislocations. Increasing CNTs concentration up to 0.6 g·L^{-1} leads to higher reduction in the coefficient of friction and improved wear resistance properties. In addition, some authors have mentioned that CNTs could help retain hardness of the composite at high temperatures, this is an important factor due to the heat generation during the wear test. Others believe that the dissociation of hydrogen and hydroxyl from water vapor and their reaction with C atoms would form a passive layer and thus decrease the coefficient of friction [35,52]. However, it should not be neglected that CNTs rolling by cutting and reconnecting SP2 covalent bonds is the main reason for the improved wear behavior which prevented direct contact with the counterpart [53]. At the initiation of the wear test period, it was witnessed that for both as-plated and plasma-nitrided Ni-B-1 g·L^{-1} CNT samples, the coefficient of friction increased.

Table 5
Results of average coefficient of friction, mass loss and specific wear rate of coated samples.

Sample	Coefficient of friction	Mass loss (mg)	Specific wear rate (kg/N·m) × 10^{-6}
Ni-B as-plated	0.6943	3.5	7E−4
Ni-B-0.2 g·L^{-1} CNT as-plated	0.5901	2.4	4.8E−4
Ni-B-0.6 g·L^{-1} CNT as-plated	0.5143	2.1	4.2E−4
Ni-B-1 g·L^{-1} CNT as-plated	0.5468	2.8	5.6E−4
Ni-B plasma nitrided	0.5424	1.9	3.8E−4
Ni-B-0.2 g·L^{-1} CNT plasma-nitrided	0.4765	1.6	3.2E−4
Ni-B-0.6 g·L^{-1} CNT plasma-nitrided	0.3352	1.2	2.4E−4
Ni-B-1 g·L^{-1} CNT plasma-nitrided	0.4651	1.7	3.4E−4

However, in plasma-nitrided sample after an about 100 m sliding distance the coefficient of friction was declined (Fig. 13d). This is mainly affiliated with separation of the poor coherent conglomerate particles which nucleated and grew during CNTs agglomeration, and due to the high microhardness of sample, more shear stress or sliding distance is needed to remove these particles.

Table 5 shows the average coefficient of friction and specific wear rate of both as-plated and plasma-nitrided samples. It can be observed that the friction coefficient has a direct relation with the specific wear rate. Plasma-nitrided Ni-B-0.6 g·L^{-1} CNT had the lowest specific wear rate in comparison with the other samples due to several reasons such as higher microhardness, lower coefficient of friction, smaller grain size and most importantly homogenous distribution of Ni_2B, Ni_3B and BN particles.

Fig. 14 illustrates FESEM analysis of the samples worn surfaces. In Ni-B as-plated sample lamellar debris particles indicate the delamination occurred during the wear test (Fig. 14a). The high solubility of iron from the counterpart in nickel from the coated surface resulted in successive welding and detaching of surface and counterpart which ultimately caused delamination in the sample. As has been reported by numerous researchers, abrasion and adhesion might be the main mechanism affecting the sample [54,55]. By increasing the CNTs concentration up to 0.6 g·L^{-1} fine grooves along the sliding direction, was observed (Fig. 14b, c). According to Fig. 15, Chemical analysis of the elements remained on the wear track illustrated a decreased amount of iron in comparison with Ni-B sample. This might be due to the fact that the cut off CNTs act as ball bearing spacer and could prevent direct contact of the coated surface and the counterpart and thus the diffusion of the iron element into the coated surface could decrease [52]. Therefore, by increasing the concentration of CNTs up to 0.6, due to the presence of a more lubricated surface, the contact of the surface and the counterpart lessens and the wear resistance could increase. Studying Ni-B-1 g·L^{-1} CNT sample (Fig. 14d), deeper groves were observed owing to the separation of conglomerate particles that had weak bonding energy with the surface during the wear test [56].

Microfractures and particles flaking off from the surface were observed in Ni-B plasma-nitrided sample (Fig. 14e). Due to higher hardness of the sample, the shear stress and friction heating between the counterpart and the coated surface were larger which resulted in higher oxidation of the surface. The EDS results proves that the amount of oxygen in the plasma-nitrided Ni-B-CNT samples was lower in comparison with the Ni-B sample. This could be ascribed to the fact that CNTs could prevent excessive heat generation during the wear test; thus, the plastic deformation was decreased and a smooth surface with fine grooves and lower debris were observed in the FESEM images

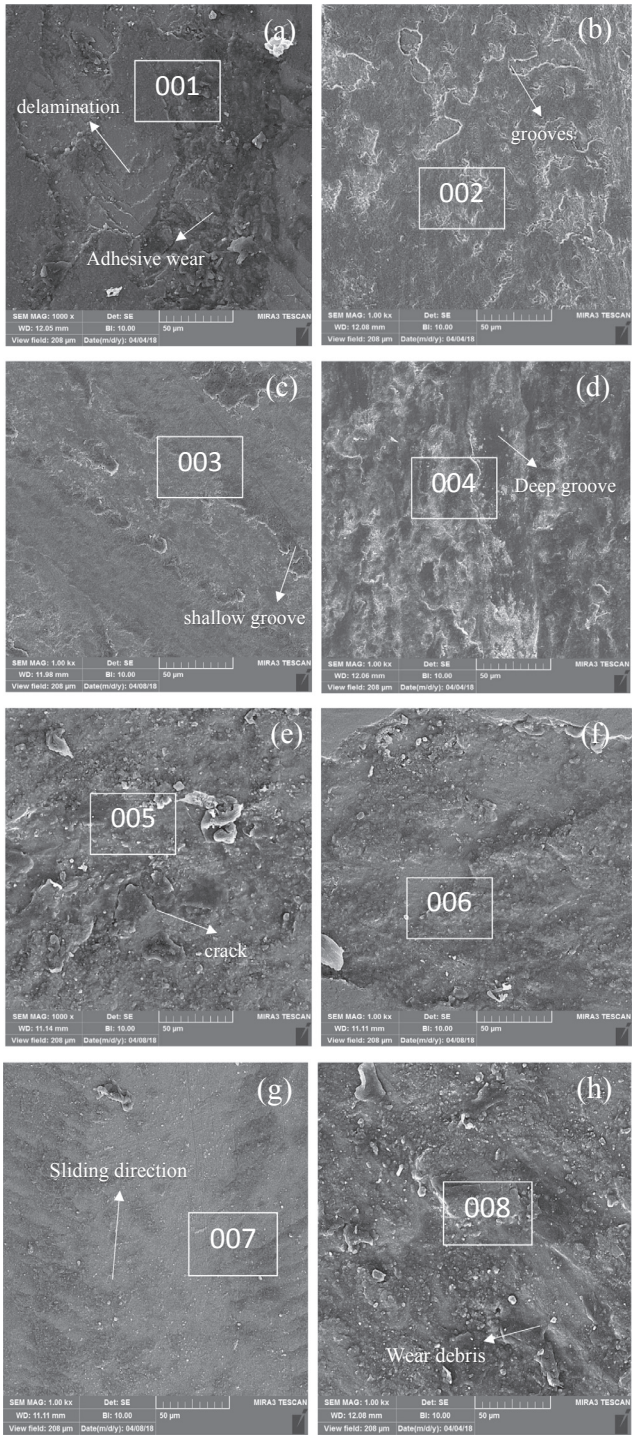

Fig. 14. FESEM micrographs of worn surfaces of the (a) Ni-B, (b) Ni-B-0.2 g·L^{-1} CNT, (c) Ni-B-0.6 g·L^{-1} CNT, (d) Ni-B-1 g·L^{-1} CNT as-plated, and (e) Ni-B, (f) Ni-B-0.2 g·L^{-1} CNT, (g) Ni-B-0.6 g·L^{-1} CNT, (h) Ni-B-1 g·L^{-1} CNT plasma-nitrided samples.

(Fig. 14f, g). Higher microhardness values and the uniform distribution of particles in Ni matrix which helped transfer the counterpart force from Ni to the CNTs ultimately resulted in higher wear resistance in the

plasma-nitrided Ni-B-0.6 g·L^{-1} CNT sample [52]. Moreover, lower grain size in comparison with the other plasma-nitrided samples, caused the grain peeling mechanism to be decreased owing to high interfacial strength [57], was another reason why Ni-B-0.6 g·L^{-1} CNT had the smoothest wear trace (Fig. 14g). Studying the Ni-B-1 g·L^{-1} CNT sample, indicated that the presence of fine debris after the wear test can be ascribed to the coarse particles cut from the surface and crushed due to the pin continuously move on the surface (Fig. 14h). The particles movement leaves some scratch on the surface of the sample which ultimately reduces the wear properties.

4. Conclusions

In the present work, the wear behavior of the as-plated and plasma-nitrided Ni-B-CNT coatings was taken into investigation. The results indicated that carbon nanotubes could effectively influence the crystallographic structure of Ni-B electroless through facilitating the Ni nucleation. Increasing the CNTs concentration led to a transition from amorphous to semi-crystalline structure.

Homogenous CNTs distribution changed the morphology of the coated surface by filling the crevices and cracks formed during the hydrogen evolution reaction. CNTs restraining crystal and particle growth resulted in the formation of small nodules except for the Ni-B-1 g·L^{-1} CNT sample in which agglomeration occurred due to the high level of CNTs concentration and therefore a value of higher surface roughness was achieved.

Increasing CNTs concentration in as-plated samples caused the friction coefficient and the specific wear rate to fall which was mainly due to the self-lubricating mechanism of CNTs. In the Ni-B-1 g·L^{-1} CNT, owing to the non-uniform distribution and agglomeration of CNTs, the friction coefficient increased. Plasma nitriding of electroless Ni–B and Ni-B-CNT, resulted in the interstitial diffusion of nitrogen atoms in the Ni matrix and formation of Ni_3B, Ni_2B and BN phases, therefore, the microhardness increased.

The presence of CNTs decreased the plastic deformation in plasma-nitrided samples, as excessive heat generation was prevented during the wear test. Therefore, the wear resistance was improved. The highest wear resistance belonged to the Ni-B-0.6 g·L^{-1} CNT sample. This could be affiliated to the lower grain size, higher microhardness and uniform distribution of the CNTs.

Since, only a handful of studies have investigated the heat treatment of nickel-boron coatings using the plasma-nitriding treatment, and also as CNTs have not yet been applied as nanocomposite in nickel-boron coating the present investigation could pave the way to further research.

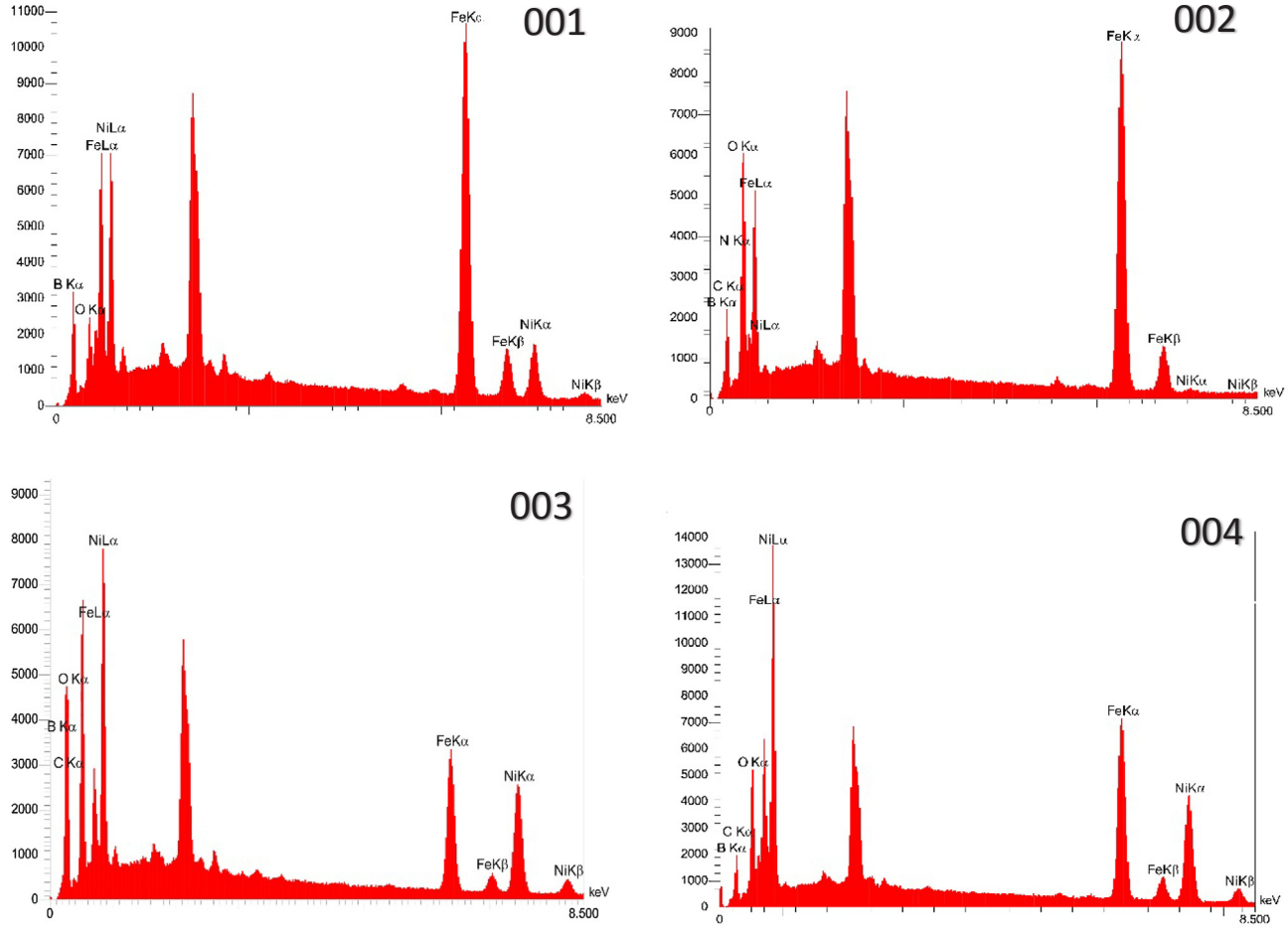

Fig. 15. EDS analysis of worn surface of samples.

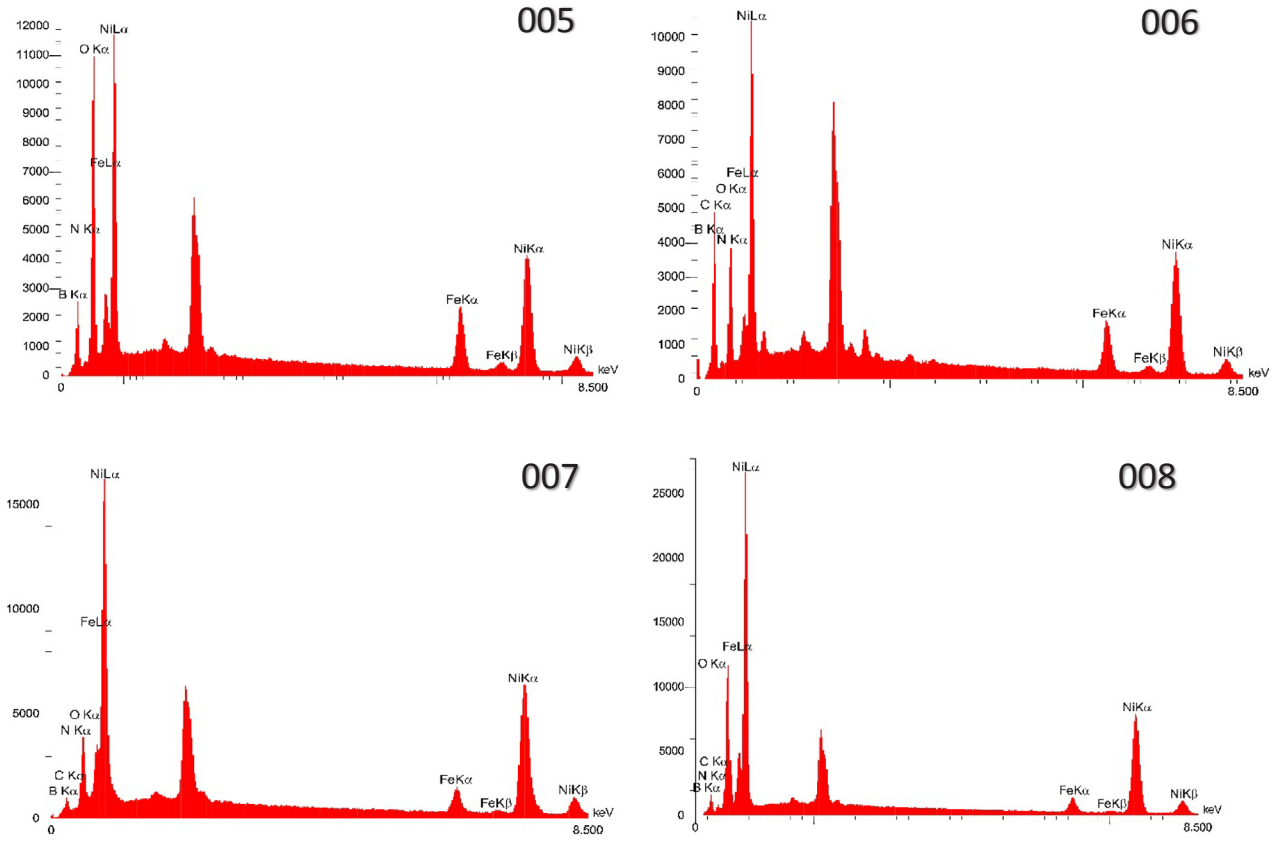

Fig. 15. (*continued*)

References

[1] Z.A. Hamid, H. Hassan, A. Attyia, Influence of deposition temperature and heat treatment on the performance of electroless Ni–B films, Surface Coat. Technol. 205 (2010) 2348–2354.

[2] Q.-L. Rao, G. Bi, Q.-H. Lu, H.-W. Wang, X.-L. Fan, Microstructure evolution of electroless Ni-B film during its depositing process, Appl. Surf. Sci. 240 (2005) 28–33.

[3] P. Sahoo, S.K. Das, Tribology of electroless nickel coatings – a review, Mater. Des. 32 (2011) 1760–1775.

[4] V. Vitry, L. Bonin, Formation and characterization of multilayers borohydride and hypophosphite reduced electroless nickel deposits, Electrochim. Acta 243 (2017) 7–17.

[5] V. Vitry, L. Bonin, Increase of boron content in electroless nickel-boron coating by modification of plating conditions, Surf. Coat. Technol. 311 (2017) 164–171.

[6] F. Madah, C. Dehghanian, A.A. Amadeh, Investigations on the wear mechanisms of electroless Ni–B coating during dry sliding and endurance life of the worn surfaces, Surf. Coat. Technol. 282 (2015) 6–15.

[7] A. Mukhopadhyay, T.K. Barman, P. Sahoo, Tribological behavior of sodium borohydride reduced electroless nickel alloy coatings at room and elevated temperatures, Surf. Coat. Technol. 321 (2017) 464–476.

[8] M. Anik, E. Körpe, E. Şen, Effect of coating bath composition on the properties of electroless nickel–boron films, Surf. Coat. Technol. 202 (2008) 1718–1727.

[9] V. Vitry, A.-F. Kanta, F. Delaunois, Mechanical and wear characterization of electroless nickel-boron coatings, Surf. Coat. Technol. 206 (2011) 1879–1885.

[10] Y. Wan, Y. Yu, L. Cao, M. Zhang, J. Gao, C. Qi, Corrosion and tribological performance of PTFE-coated electroless nickel boron coatings, Surf. Coat. Technol. 307 (2016) 316–323.

[11] E. Georgiza, V. Gouda, P. Vassiliou, Production and properties of composite electroless Ni-B-SiC coatings, Surf. Coat. Technol. 325 (2017) 46–51.

[12] V. Vitry, A.-F. Kanta, J. Dille, F. Delaunois, Structural state of electroless nickel–boron deposits (5 wt.% B): characterization by XRD and TEM, Surface Coat. Technol. 206 (2012) 3444–3449.

[13] A.-F. Kanta, V. Vitry, F. Delaunois, Effect of thermochemical and heat treatments on electroless nickel–boron, Mater. Lett. 63 (2009) 2662–2665.

[14] V. Vitry, A.-F. Kanta, F. Delaunois, Application of nitriding to electroless nickel–boron coatings: chemical and structural effects; mechanical characterization; corrosion resistance, Mater. Des. 39 (2012) 269–278.

[15] O.R. Monteiro, S. Murugesan, V. Khabashesku, Electroplated Ni–B films and Ni–B metal matrix diamond nanocomposite coatings, Surf. Coat. Technol. 272 (2015) 291–297.

[16] V. Niksefat, M. Ghorbani, Mechanical and electrochemical properties of ultrasonic-assisted electroless deposition of Ni–B–TiO_2 composite coatings, J. Alloy. Compd. 633 (2015) 127–136.

[17] P. Wu, H. Du, X. Chen, Z. Li, H. Bai, E. Jiang, Influence of WC particle behavior on the wear resistance properties of Ni–WC composite coatings, Wear 257 (2004) 142–147.

[18] L. Chen, L. Wang, Z. Zeng, T. Xu, Influence of pulse frequency on the microstructure and wear resistance of electrodeposited Ni–Al_2O_3 composite coatings, Surf. Coat. Technol. 201 (2006) 599–605.

[19] M. Mu, X. Zhou, Q. Xiao, J. Liang, X. Huo, Preparation and tribological properties of self-lubricating TiO_2/graphite composite coating on Ti6Al4V alloy, Appl. Surf. Sci. 258 (2012) 8570–8576.

[20] Y. He, S. Wang, F. Walsh, Y.-L. Chiu, P. Reed, Self-lubricating Ni-P-MoS_2 composite coatings, Surf. Coat. Technol. 307 (2016) 926–934.

[21] L.Y. Wang, J. Tu, W. Chen, Y. Wang, X. Liu, C. Olk, D. Cheng, X. Zhang, Friction and wear behavior of electroless Ni-based CNT composite coatings, Wear 254 (2003) 1289–1293.

[22] C. Carpenter, P. Shipway, Y. Zhu, Electrodeposition of nickel-carbon nanotube nanocomposite coatings for enhanced wear resistance, Wear 271 (2011) 2100–2105.

[23] L. Vaisman, H.D. Wagner, G. Marom, The role of surfactants in dispersion of carbon nanotubes, Adv. Colloid Interface Sci. 128 (2006) 37–46.

[24] M. Jagannatham, S. Sankaran, P. Haridoss, Microstructure and mechanical behavior of copper coated multiwall carbon nanotubes reinforced aluminum composites, Mater. Sci. Eng., A 638 (2015) 197–207.

[25] W.M. Daoush, B.K. Lim, C.B. Mo, D.H. Nam, S.H. Hong, Electrical and mechanical properties of carbon nanotube reinforced copper nanocomposites fabricated by electroless deposition process, Mater. Sci. Eng., A 513 (2009) 247–253.

[26] G. Hatipoglu, M. Kartal, M. Uysal, T. Cetinkaya, H. Akbulut, The effect of sliding speed on the wear behavior of pulse electro Co-deposited Ni/MWCNT nano-composite coatings, Tribol. Int. 98 (2016) 59–73.

[27] M.-F. Yu, O. Lourie, M.J. Dyer, K. Moloni, T.F. Kelly, R.S. Ruoff, Strength and breaking mechanism of multiwalled carbon nanotubes under tensile load, Science 287 (2000) 637–640.

[28] P.-C. Tsai, Y.-R. Jeng, J.-T. Lee, I. Stachiv, P. Sittner, Effects of carbon nanotube reinforcement and grain size refinement mechanical properties and wear behaviors of carbon nanotube/copper composites, Diam. Relat. Mater. 74 (2017) 197–204.

[29] S. Suarez, A. Rosenkranz, C. Gachot, F. Mücklich, Enhanced tribological properties of MWCNT/Ni bulk composites – influence of processing on friction and wear behaviour, Carbon 66 (2014) 164–171.

[30] P. Hvizdoš, V. Puchý, A. Duszová, J. Dusza, C. Balázsi, Tribological and electrical properties of ceramic matrix composites with carbon nanotubes, Ceram. Int. 38 (2012) 5669–5676.

[31] L. Melk, J.J.R. Rovira, M.-L. Antti, M. Anglada, Coefficient of friction and wear resistance of zirconia–MWCNTs composites, Ceram. Int. 41 (2015) 459–468.

[32] Q. Wang, M. Callisti, A. Miranda, B. McKay, I. Deligkiozi, T.K. Milickovic, A. Zoikis-Karathanasis, K. Hrissagis, L. Magagnin, T. Polcar, Evolution of structural, mechanical and tribological properties of Ni–P/MWCNT coatings as a function of annealing temperature, Surf. Coat. Technol. 302 (2016) 195–201.
[33] V. Puchy, P. Hvizdos, J. Dusza, F. Kovac, F. Inam, M. Reece, Wear resistance of Al_2O_3–CNT ceramic nanocomposites at room and high temperatures, Ceram. Int. 39 (2013) 5821–5826.
[34] B. Munkhbayar, M.J. Nine, J. Jeoun, M. Bat-Erdene, H. Chung, H. Jeong, Influence of dry and wet ball milling on dispersion characteristics of the multi-walled carbon nanotubes in aqueous solution with and without surfactant, Powder Technol. 234 (2013) 132–140.
[35] M. Zhou, Y. Mai, H. Ling, F. Chen, W. Lian, X. Jie, Electrodeposition of CNTs/copper composite coatings with enhanced tribological performance from a low concentration CNTs colloidal solution, Mater. Res. Bull. 97 (2018) 537–543.
[36] S. Javadian, A. Motaee, M. Sharifi, H. Aghdastinat, F. Taghavi, Dispersion stability of multi-walled carbon nanotubes in catanionic surfactant mixtures, Colloids Surf., A 531 (2017) 141–149.
[37] M.D. Clark, S. Subramanian, R. Krishnamoorti, Understanding surfactant aided aqueous dispersion of multi-walled carbon nanotubes, J. Colloid Interface Sci. 354 (2011) 144–151.
[38] T.A. Saleh, The influence of treatment temperature on the acidity of MWCNT oxidized by HNO 3 or a mixture of HNO_3/H_2SO_4, Appl. Surface Sci. 257 (2011) 7746–7751.
[39] Y.-C. Chiang, W.-H. Lin, Y.-C. Chang, The influence of treatment duration on multi-walled carbon nanotubes functionalized by H_2SO_4/HNO_3 oxidation, Appl. Surf. Sci. 257 (2011) 2401–2410.
[40] A. Osorio, I. Silveira, V. Bueno, C. Bergmann, H_2SO_4/HNO_3/HCl—functionalization and its effect on dispersion of carbon nanotubes in aqueous media, Appl. Surf. Sci. 255 (2008) 2485–2489.
[41] J.-H. Ahn, H.-S. Shin, Y.-J. Kim, H. Chung, Structural modification of carbon nanotubes by various ball milling, J. Alloys Compd. 434 (2007) 428–432.
[42] B. Krause, T. Villmow, R. Boldt, M. Mende, G. Petzold, P. Pötschke, Influence of dry grinding in a ball mill on the length of multiwalled carbon nanotubes and their dispersion and percolation behaviour in melt mixed polycarbonate composites, Compos. Sci. Technol. 71 (2011) 1145–1153.
[43] K.A. Wepasnick, B.A. Smith, K.E. Schrote, H.K. Wilson, S.R. Diegelmann, D.H. Fairbrother, Surface and structural characterization of multi-walled carbon nanotubes following different oxidative treatments, Carbon 49 (2011) 24–36.
[44] A.B. Porto, L.F.C. de Oliveira, H.F. Dos Santos, Exploring the potential energy surface for reaction of SWCNT with NO^{2+}: a model reaction for oxidation of carbon nanotube in acid solution, Comput. Theor. Chem. 1088 (2016) 1–8.
[45] V. Likodimos, T.A. Steriotis, S.K. Papageorgiou, G.E. Romanos, R.R. Marques, R.P. Rocha, J.L. Faria, M.F. Pereira, J.L. Figueiredo, A.M. Silva, Controlled surface functionalization of multiwall carbon nanotubes by HNO_3 hydrothermal oxidation, Carbon 69 (2014) 311–326.
[46] U. Tocoglu, M. Alaf, O. Cevher, M. Guler, H. Akbulut, The effect of oxidants on the formation of multi-walled carbon nanotube buckypaper, J. Nanosci. Nanotechnol. 12 (2012) 9169–9174.
[47] Y.N. Bekish, S. Poznyak, L. Tsybulskaya, T. Gaevskaya, Electrodeposited Ni–B alloy coatings: structure, corrosion resistance and mechanical properties, Electrochim. Acta 55 (2010) 2223–2231.
[48] R. Karslioglu, H. Akbulut, Comparison microstructure and sliding wear properties of nickel–cobalt/CNT composite coatings by DC, PC and PRC current electrodeposition, Appl. Surface Sci. 353 (2015) 615–627.
[49] V. Vitry, A. Sens, A.-F. Kanta, F. Delaunois, Experimental study on the formation and growth of electroless nickel–boron coatings from borohydride-reduced bath on mild steel, Appl. Surf. Sci. 263 (2012) 640–647.
[50] J. Umeda, B. Fugetsu, E. Nishida, H. Miyaji, K. Kondoh, Friction behavior of network-structured CNT coating on pure titanium plate, Appl. Surf. Sci. 357 (2015) 721–727.
[51] D.-E. Kim, C.-L. Kim, H.-J. Kim, A novel approach to wear reduction of micro-components by synthesis of carbon nanotube-silver composite coating, CIRP Ann.-Manuf. Technol. 60 (2011) 599–602.
[52] M.M. Bastwros, A.M. Esawi, A. Wifi, Friction and wear behavior of Al–CNT composites, Wear 307 (2013) 164–173.
[53] M. Alishahi, S.M. Monirvaghefi, A. Saatchi, S.M. Hosseini, The effect of carbon nanotubes on the corrosion and tribological behavior of electroless Ni–P–CNT composite coating, Appl. Surf. Sci. 258 (2012) 2439–2446.
[54] E. Correa, A.A. Zuleta, L. Guerra, M.A. Gómez, J.G. Castaño, F. Echeverría, H. Liu, P. Skeldon, G.E. Thompson, Tribological behavior of electroless Ni–B coatings on magnesium and AZ91D alloy, Wear 305 (2013) 115–123.
[55] G. Yamamoto, K. Shirasu, Y. Nozaka, Y. Sato, T. Takagi, T. Hashida, Structure–property relationships in thermally-annealed multi-walled carbon nanotubes, Carbon 66 (2014) 219–226.
[56] I.-Y. Kim, J.-H. Lee, G.-S. Lee, S.-H. Baik, Y.-J. Kim, Y.-Z. Lee, Friction and wear characteristics of the carbon nanotube–aluminum composites with different manufacturing conditions, Wear 267 (2009) 593–598.
[57] W. Zhai, N. Srikanth, L.B. Kong, K. Zhou, Carbon nanomaterials in tribology, Carbon 119 (2017) 150–171.